Influences of Structural Modification of Naphthalenediimides with Benzothiazole on Organic Field-Effect Transistor and Non-Fullerene Perovskite Solar Cell Characteristics

Dada B. Shaikh, [a],[b]† Ahmed Ali Said,[c]† Zongrui Wang,[c] Pedada Srinivasa Rao,[a],[b] Rajesh S. Bhosale, [a]‡ Adrian M. Mak,[d] Kexiang Zhao,[c] Yu Zhou,[e] Wenbo Liu,[c] Weibo Gao,[e] Sidhanath V. Bhosale,*[a],[b] Sheshanath V. Bhosale,*[f] and Qichun Zhang*[c]

Abstract: Developing air-stable high-performance n-type and ambipolar organic field effect transistors (OFETs) is very important and highly desirable. In this investigation, we designed and synthesized two naphthalenediimide (NDI) derivatives (NDI-BTH1 and NDI-BTH2), nd found that introduction of 2-(benzo[d]thiazol-2-yl) acetonitrile groups at NDI core position gave lowest unoccupied molecular orbital (LUMO, -4.326 eV) and displayed strong electron affinities, suggesting that NDI-BTH1 might be a promising electron transporting material (i.e. n-type semiconductor). Whereas, NDI-BTH2 bearing bis(benzo[d]thiazol-2-yl)methane at NDI core with LUMO of -4.243 eV was demonstrated to be ambipolar material. OFET based on NDI-BTH1 and NDI-BTH2 have been fabricated and the charge carrier mobility of NDI-BTH1 and NDI-BTH2 are 14.00 x 10^{-5} cm^2/Vs (μ_e) and 8.64 x 10^{-4} cm^2/Vs (μ_e)/ 1.68 x 10^{-4} cm^2/Vs (μ_h) respectively. Moreover, a difference in NDI-core substituent moieties significantly alters the UV-vis absorption and cyclic voltammeter properties. We further successfully employed NDI-BTH1 and NDI-BTH2 as electron transport layer (ETL) materials in inverted perovskite solar cells (PSCs). The PSC performance exhibits that NDI-BTH2 as ETL material gave power conversion efficiency (PCE) of 15.4%, while NDI-BTH1 as ETL material obtained PCE of 13.7%. The performance of PSCs is in agreement with the OFET results. We presume that improvement in solar cell efficiency of NDI-BTH2-based PSCs is due to increase in number of sulphur atoms in the molecular framework, which enhances the passivation power toward electron trap states on the perovskite layer surface and the binding between the lead of perovskite and the ETL, as well as the well-matched LUMO of NDI-BTH2 toward conduction band of perovskite layer, which in turn enhance electron extraction and transportation from the perovskite layer.

[a, b] Mr. D. B. Shaikh, Dr. P. S. Rao, Dr. R. S. Bhosale and Dr. S. V. Bhosale
Polymers and Functional Material Division, CSIR-Indian Institute of Chemical Technology, Hyderabad-500007, Telangana, India
Academy of Scientific and Innovative Research (AcSIR), Gaziabad-201002, Uttar Pradesh, India
E-mail: bhosale@iict.res.in

[c] Mr. A. Ali Said, Dr. Z. Wang, Mr. K. Zhao, W. Liu and Prof. Q. Zhang
School of Materials Science and Engineering, Nanyang Technological University, 50 Nanyang Avenue-639798, Singapore.
E-mail: qczhang@ntu.edu.ac

[d] Institute of High Performance Computing, 1 Fusionopolis Way #16-16, Connexis, Singapore 138632.

[e] Mr. Y. Zhou and Mr. W. Gao
Division of Physics and Applied Physics, School of Physical and Mathematical Sceinecs, Nanyang Technological University, 50 Nanyang Avenue-639798, Singapore.

[f] Prof. S. V. Bhosale
School of Chemical Sciences
Goa University, Taleigao Plateau, Goa-403206, India
Email: svbhosale@unigoa.ac.in

† These authors contributed equally.

Supporting information for this article is given via a link at the end of the document.((Please delete this text if not appropriate))

Introduction

The market demand for developing efficient organic semiconducting materials is rapidly increasing due to their tremendous usage in optoelectronic devices such as organic field-effect transistors (OFETs), organic light-emitting diodes (OLEDs) and photovoltaic solar cell applcations.[1] In OFETs, the p-type semiconductors with excellent hole mobilities and air stabilities are largely investigated.[2] However, as the counterpart of p-type materials, air-stable high-performance n-type semiconducting materials are less explored due to their difficult synthesis, poorer water and air stabilities, and lower field-effect mobilities.[3] Therefore, there is an urgent demand to prepare these materials and fabricate high performance air stable n-type OFETs.

Meanwhile, dramatic progress has been also witnessed for n-type semiconducting materials with the electron mobility values approaching 11 cm^2/Vs at ambient and inert atmosphere.[4] Moreover, it is notable that as compared to p- and n-type semiconducting materials, ambipolar organic semiconductors, which exhibit high and balanced hole/electron mobilities, are lagging behind,[5] although ambipolar semiconductor materials are also very important for the fabrication of complementary digital integrated circuits and light emitting field-effect transistors.[6]

Recent research studies in the field of perovskite solar cells (PSCs)[7] have revealed that n-type semiconducting materials have a significant potential as non-fullerene ETL to approach high performance PSCs.[8-10] Literature search demonstrated that the phenyl-C_{61}-butyric acid methyl ester (PCBM) based PSCs exhibits ~18% efficiency.[11-13] The PSCs with PCBM as ETL suffers some difficulties due to their poor solubility, lower thermal stability and face segregation.[12,13] To overcome these difficulties, scientists come up with small molecules and polymers as non-

fullerene ETLs.[14] Compared with PCBM as ETL in PSCs, n-type semiconducting small organic molecules and polymers can offer promising ETLs because of their tunable absorption range and the energy levels.[8c, 14] As a result, such n-type ETL materials are able to easily align device fabrication and efficiently extract and transport electrons from perovskite to electrode materials. In addition, n-type semiconducting organic small molecules are preferable compared to n-type polymers due to their good molecular packing as well as monodispersity in the ETL layer.[15]

In recent years, many n-type semiconducting small molecules such as azaacene,[16] hexaazatrinaphthylene,[17] perylenediimides (PDI),[18] diketopyrrolopyrrole (DPP)-isoindigo conjugate,[19] hexatrinaphtho[2,3-c][1,2,5]thiadiazole (HATNT),[20] coronene-type diimide,[21] and NDIs[22] were employed as an efficient ETL in PSCs. In inverted PSCs, among the various n-type ETL material, NDI based small molecules offer significant merits such as good thermal stability, easy solution processability, high solubility in common organic solvents and high electron mobility (1.2 $cm^2V^{-1}s^{-1}$).[23] Although NDI-based small molecule displayed remarkable values, there are very few reports in literature on NDI derivative used as ETL. Therefore, there is good opportunity to develop NDI-based novel small organic molecular design with the enhanced electron-transporting ability and their applications in PSCs.

Very recently, benzothiazole in conjugation with DPP molecular design has been introduced for semiconducting OFETs.[24] As-fabricated benzothiazole-DPP-based organic transistor device exhibits good hole-transport mobility (0.011 cm^2/Vs).[24] Despite their good OFET properties, it is rarely employed to fabricate organic semiconductors and their use in PSCs. As a result, it is an urgent task to explore benzothiazole based small organic molecules with particular attention to the ETL for PSCs.

In this study, we synthesized two novel NDI chromophores such as (2E,2'E)-3,3'-(5,5'-(2,7-dioctyl-1,3,6,8-tetraoxo-1,2,3,6,7,8-hexahydrobenzo[lmn][3,8]phenanthroline-4,9-diyl)bis(thiophene-5,2-diyl))bis(2-(benzo[d]thiazol-2-yl)acrylonitrile)[NDI-BTH1] and 4,9-bis(5-(2,2-bis(benzo[d]thiazol-2-yl)vinyl) thiophen-2-yl)-2,7-dioctylbenzo[lmn][3,8]phenanthroline-1,3,6,8 (2H,7H)-tetraone [NDI-BTH2] consisting of 2-(benzo[d]thiazol-2-yl)acetonitrile and bis(benzo[d]thiazol-2-yl)methane, respectively. The energy levels of NDI-BTH1 and NDI-BTH2 are systematically tuned to achieve good electron mobilities. NDI-BTH1 exhibits n-type semiconducting properties whereas NDI-BTH2 displayed ambipolar characteristics. The effect of the NDI core modification on solar cell performance was also studied using PEDOT:PSS as the hole transporting layer (HTL), perovskite $FA_yMA_{1-y}PbI_{3-x}Cl_x$ as the light absorber and NDI-BTH1 and NDI-BTH2 as ETLs in inverted p-i-n PSCs. NDI-BTH1 as ETL exhibits the PCEs of 13.7%. Whereas, the highest efficiency up to 15.4% value was obtained with NDI-BTH2 as ETL materials. It was noted that the inverted PSCs performance based on NDI-BTH2 (η = 15.4%) as ETL is higher than that of PSCs based on NDI-BTH1 (η = 13.7%). This was attributed to the broader light absorption, ambipolar properties of NDI-BTH2 and more Pb-S binding between perovskite and ETL.

Results and Discussion

To utilize the NDI-based new non-fullerene ETL materials in inverted p-i-n architecture of PSCs, we first designed the organic molecules based on the optoelectronic properties of chromophores used in it. We designed acceptor-donor-acceptor-donor-acceptor (A-D-A-D-A), NDI-BTH1 and NDI-BTH2, conjugates by comprising electron deficient (A) 2-(benzo[d]thiazol-2-yl)acetonitrile/bis(benzo[d]thiazol-2-yl) methane, electron rich (D) thiophene and electron deficient (A) NDIs and are depicted in Scheme 1.

In our molecular design, we chose NDI as a core subunit based on following literature reported merits such as (i) NDI is a planar n-type semiconducting π-conjugated system, (ii) exhibits high thermal stability, (iii) displays excellent electron mobilities, and (iv) shows tunable light absorption properties.[25] Furthermore, we utilized benzothiazole subunit at NDI core because it possessed the following properties: (i) it can enhance the π-conjugation length, (ii) the increase in conjugation may enhance intermolecular π-π stacking interactions, (iii) the LUMO energy levels of NDI-BTH1 and NDI-BTH2 are expected to be lower due to their electron withdrawing properties, and (iv) such low LUMO materials can exhibit air-stable n-type semiconducting properties. Moreover, we believe that the incorporation of 2-(benzo[d]thiazol-2-yl)acetonitrile and bis(benzo[d]thiazol-2-yl)methane into NDI molecular architecture can enhance the binding between ETL and perovskite layer through S-Pb or S-I interactions in p-i-n PSCs.[26] We imagined that, both NDI-BTH1 and NDI-BTH2 molecular entities can be employed as new building blocks to prepare ETL materials, which can facilitate electron extraction from perovskite and transportation to electrode materials in solution-processed PSCs.

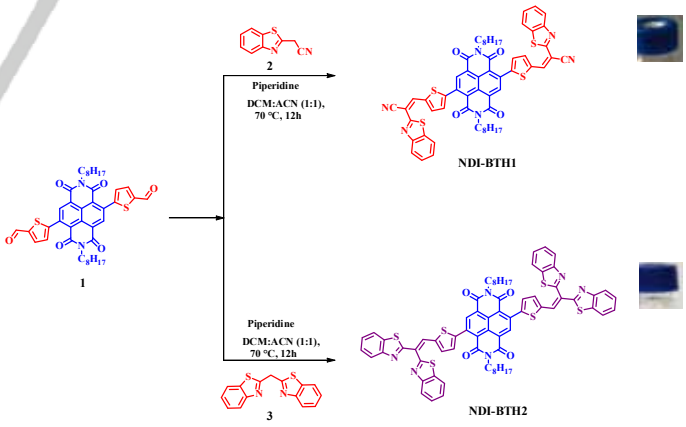

Scheme 1. Synthetic pathway of NDI-BTH1 and NDI-BTH2

The synthetic pathway of new NDI based non-fullerene organic molecules NDI-BTH1 and NDI-BTH2 is shown in Scheme 1. The 5,5'-(2,7-dioctyl-1,3,6,8-tetraoxo-1,2,3,6,7,8-hexahydrobenzo [lmn][3,8]phenanthroline-4,9-diyl)bis(thiophene-2-carbaldehyde) **1** was synthesized according to the procedure reported in literature.[27] NDI-BTH1 and NDI-BTH2 were prepared by the

piperidine-catalysed Knoevenagel condensation reactions in CH_2Cl_2: CH_3CN (1:1) solvent mixture (Scheme 1, see the details in the experimental section). The reaction between **1** and **2** as well as **1** and **3** resulted into NDI-BTH1 (64.76%) and NDI-BTH2 (72.57%), respectively. The as-synthesized compounds were purified by silica gel column chromatography. The chemical structures of NDI-BTH1 and NDI-BTH2 were established and confirmed by FT-IR, ^{1}H NMR, ^{13}C NMR and MALDI-TOF data (See experimental section and Figure S1 to S12 Supporting Information).

Thermal gravimetric analysis (TGA) was employed to investigate the thermal stability of NDI-BTH1 and NDI-BTH2 at the heating rate of 10 °C/min under a nitrogen atmosphere. TGA exhibited good thermal stabilities of NDI-BTH1 and NDI-BTH2 with the 5% weight loss temperatures (T_d) over 396 °C and 318 °C, respectively (Figure S13 and S14, †SI). Compound NDI-BTH2 exhibited two weight loss temperatures at 318 °C and 435 °C, suggesting that this compound undergoes two decomposition processes. The good thermal stability of NDI-BTH1 and NDI-BTH2 provided a base for wide range of thermal annealing for the device optimization of OFETs and PSCs. The as-obtained NDI-BTH1 and NDI-BTH2 show the melting points at 214-216 °C and 240-242 °C, respectively, indicating both chromophores are stable enough for device fabrications.

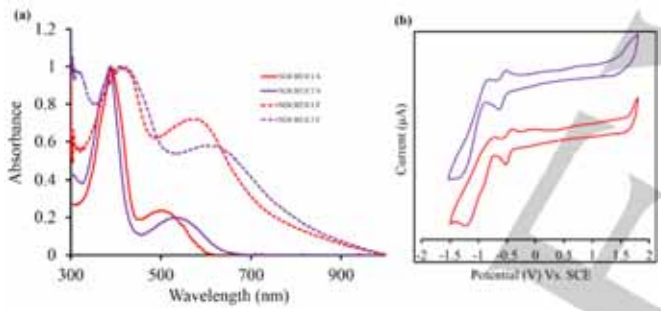

Figure 1. (a) UV-vis absorption spectra in dichloromethane (1 x 10^{-5} M); (b) cyclic voltammograms of NDI-BTH1 (red line) and NDI-BTH2 (violet line) in dichloromethane (5 x 10^{-4} M)

The UV-vis absorption spectra of NDI-BTH1 and NDI-BTH2 in solution state as well as thin-film state were depicted in Figure 1a. The UV-vis spectra of NDI-BTH1 exhibited two maxima absorption peaks at 395 nm and 510 nm, whereas the optical absorption of their thin-film showed peaks at 415 nm and 580 nm. The absorption of NDI-BTH1 in thin-film exhibited 20 nm and 70 nm bathochromic-shifts while NDI-BTH2 showed two maximum absorption band wavelengths at 384 nm and 540 nm in solution state as shown in Figure 1a. The thin-film state of NDI-BTH2 displayed absorption maxima wavelengths at 426 nm and 625 nm with red-shift of 42 nm and 85 nm. NDI-BTH2 thin-film state exhibited greater bathochromic shifts compared to those of NDI-BTH1, which suggests that the flanked benzothiazole facilitates stronger π-π interaction. The higher energy absorption peak at 300-500 nm can be attributed to the π-π* transitions whereas the lower energy absorption band at 500-800 nm should be ascribed to the intramolecular charge transfer (ICT) effect. The bathochromic absorption spectral shifts are attributed to strong intermolecular interactions and should be instrumental for charge mobilities. The optical absorption onset wavelength (λ_{onset}) based on thin-film absorption of NDI-BTH1 and NDI-BTH2 were employed to calculate the optical band gap (E_g^{opt}= 1240/λ_{onset}) and were summarized in Table 1. The onset absorption of NDI-BTH1 and NDI-BTH2 are 750 nm and 806 nm, respectively. The estimated E_g^{opt} of NDI-BTH1 and NDI-BTH were found to be 1.653 eV and 1.538 eV, respectively. To determine LUMO energy level, cyclic voltammetry (CV) measurements of NDI-BTH1 and NDI-BTH2 were conducted in CH_2Cl_2 with 0.1 M tetrabutylammonium hexafluorophosphate and are depicted in Figure 1b and are listed in Table 1. The onset reduction potentials (E_{red}^{onset}) for NDI-BTH1 and NDI-BTH2 were determined and found to be -0.374 V and -0.457 V, respectively. Therefore, by employing the equation: E_{LUMO} = -q (E^{red}_{onset} + 4.7), the corresponding LUMO energies of NDI-BTH1 and NDI-BTH2 were estimated to be -4.326 eV and -4.243 eV, respectively (Table 1). The LUMO energy levels of NDI-BTH1 and NDI-BTH2 are lower compared to unsubstituted NDIs.[25] This may be attributed to the elongation of π-conjugation and induction of electron due to the incorporation of functional subunits. The low LUMO energies of NDI-BTH1 and NDI-BTH2 indicate that both compounds may have good electron-transporting abilities and could exhibit better performance in OFETs. By applying the equation: E_{HOMO} = E_g^{opt} + E_{LUMO}, the highest occupied molecular orbital (HOMO) energies of NDI-BTH1 and NDI-BTH2 were determined to be -5.979 eV and -5.781 eV, respectively, as shown in Table 1.

Table 1. The optical and electrochemical properties of NDI-BTH 1 and NDI-BTH 2

Compound	λ_{onset} nm	E^{ox}_{onset} (V)	E^{red}_{onset} (V)	HOMO (eV)	LUMO (eV)	$^{cv}E_g$ (eV)	$^{opt}E_g$
NDI-BTH 1	750	-----	-0.374	-5.979	-4.326	----	1.653
NDI-BTH 2	806	-----	-0.457	-5.781	-4.243	----	1.538

The theoretical calculations using the hybrid B3LYP density functional with a 6-31G(d) basis set was employed to get results of geometrical configuration and frontier molecular orbitals of NDI-BTH1 and NDI-BTH2.[28] The TD-DFT results are depicted in Figure S15 & Figure S16 and summarized in Table S1 for NDI-BTH1 and NDI-BTH2, respectively. The TD-DFT result for NDI-BTH1 exhibits three absorptions peaks, two at 403 nm and 428 nm and another at longer wavelength at 693 nm. Whereas NDI-

BTH2 displays the absorption bands at 391 nm, 419 nm and 711 nm. The absorption wavelength trend is in according to experimental results (Figure 1a). The molecular orbitals for NDI-BTH1 and NDI-BTH2 were generated at B3LYP/6-31(d) level of geometry and depicted in Figure 2 and Table S2 and S3.[28] For NDI-BTH1, the HOMO energy level is located on the benzothiazole subunits, thiophene moieties and partially on NDI core. Whereas, LUMO energy level was delocalized over NDI core, electron donating thiophene ring system and –CN functional group. For NDI-BTH2, the electronic charge distribution in HOMO is localized at the benzothiazole ring system and partially on NDI core, whereas in LUMO is located at NDI core and thiophene moieties. As shown in Figure 2 and Table S2, the HOMO and LUMO energies of NDI-BTH1 and NDI-BTH2 were calculated to be -6.23 eV/-4.13 eV and -5.90 eV/-3.86 eV, respectively. The theoretical calculations were carried out in the gas phase and thus there were HOMO/LUMO energy value differences between the calculated and those obtained *via* spectroscopic and electrochemical experimental data (Table 1). These results suggest that the modification at the NDI core with suitable functional groups can effectively manipulate their HOMO/LUMO energy levels.

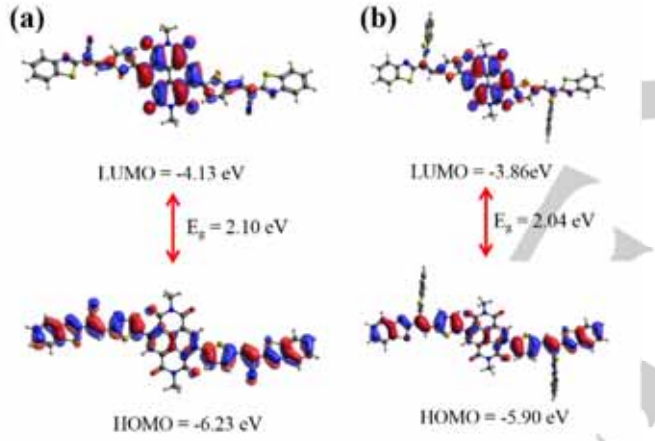

Figure 2. Frontier molecular orbitals diagram of (a) NDI-BTH1 and (b) NDI-BTH2 showing electron density distribution.

To investigate the charge transport properties of NDI-BTH 1 and NDI-BTH 2, the bottom-gate top-contact (BGTC) organic thin-film field effect transistors (OTFTs) with the *n*-octadecyltrimethoxylsilane (OTS) modified SiO_2 (300 nm, C_i = 11 nF/cm^2) as dielectric layer, the highly n-doped silicon wafer as gate electrode and the thermally-evaporated gold as source/drain electrodes were prepared. The thin-film of the molecules were obtained by spin-coating. The OFET devices of compound NDI-BTH1 and NDI-BTH2 were investigated in the air and their performances were examined after annealing at different temperatures. The transfer and output characteristics of the OFETs thin-film based on NDI-BTH1 (a, d) and NDI-BTH2 (b, e and c, f) are depicted in Figure 3 and summarized in Table 2 and 3.

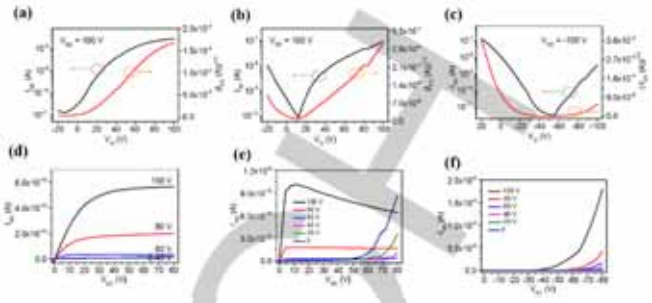

Figure 3. Transfer (top row) and output (bottom row) characteristics of organic thin-film effect transistors based on (a, d) NDI-BTH1; (b, e) NDI-BTH2 and (c, f) NDI-BTH2

The electron mobilities, on-off ratios and threshold voltages of the thin-film OFETs for NDI-BTH1 is tabulated in Table 2. The organic field-effect electron (μ_e) mobilities of NDI-BTH1 at room temperature is 6.83 x 10^{-5} cm^2/Vs with the current on/off ratios (I_{on}/I_{off}) = 10^1 and threshold voltage (V_{th}) of 2.79 V. After thermal annealing at 80 °C (Figure 3a & d, Table 2, entry 2), NDI-BTH1-based OFETs exhibits the maximum electron mobility of 14.00 x 10^{-5} cm^2/Vs with the increase in threshold voltage of 15.9 V and on-off ratio of 10^3. After further increase in annealing temperature to 140 °C (Figure 3a & d, Table 2, entry 3), the electron mobilities decreased to 7.78 x 10^{-5} cm^2/Vs with the decrease in threshold voltage to 6.02 V and on-off ratio to 10^1. We presume that the change in electron mobilities with annealing temperatures is in agreement with the changes appeared within thin film. Thus, The NDI-BTH1 based OFETs devices demonstrated n-type semiconducting properties. Furthermore, the electron (μ_e) and hole (μ_h) mobilities of thin film of NDI-BTH2 were examined and depicted in Figure 3 (b, e and c, f) and the results were listed in Table 3. The electron (μ_e) and hole (μ_h) mobilities of NDI-BTH2 at 140 °C were measured and found to be 8.64 x 10^{-4} cm^2/Vs and 1.68 x 10^{-4} cm^2/Vs, respectively. After increasing the substrate annealing temperature to 200 °C, the μ_e mobilities of NDI-BTH2 decreased and found to be 4.00 x 10^{-4} cm^2/Vs, whereas μ_h mobilities were increased and achieved as 3.11 x 10^{-4} cm^2/Vs (Table 3). Thus, the OFETs result indicated that NDI-BTH2 based device works as ambipolar-type semiconductors. We note that NDI-BTH2 based OFET devices exhibited ten-fold larger electron mobilities than that of NDI-BTH1 after annealing at 140 °C. We attributed these OFETs improved performance to the introduction of additional benzothiazole moiety, which could lead to the close packing in thin-film device fabrication. These results clearly suggest that our design strategy of NDI core modification with additional electron acceptors to manipulate the semiconducting properties is efficient.

Table 2. Organic Thin-Film Transistor Performance Parameters of NDI-BTH1 with Annealing Conditions

Temperature (℃)	Electron Mobility (cm^2/Vs)	on-off ratios I_{on}/I_{off}	Threshold Voltages V_{th} (V)
RT	6.83 (4.48) E-5	10^1	2.79
80	14.0 (8.42) E-5	10^3	15.9
140	7.78 (4.95) E-5	10^1	6.02

Table 3. Organic Thin-Film Transistor Performance Parameters of NDI-BTH2 with Annealing Conditions

Temperature (℃)	Electron Mobility (cm^2/Vs)	on-off ratios I_{on}/I_{off}	Threshold Voltages V_{th} (V)
140-n	8.64 (4.06) E-4	10^3	51.9
140-P	1.68 (1.39) E-4	10^2	-77.0
200-n	4.00 (2.91) E-4	10^1	0.33
200-p	3.11 (1.41) E-4	10^1	-24.2

To correlate and elucidate the relationship between the flanked-NDI-core modified chemical structure engineering, energy levels and charge transport properties on the PSCs performance, we fabricated and evaluated inverted p-i-n PSCs using the NDI-BTH1 and NDI-BTH2 as ETL materials. NDI-BTH1 and NDI-BTH2 were employed as ETLs due to their HOMO and LUMO level suitability to extract electrons from the perovskite layer and transport to the electrode.

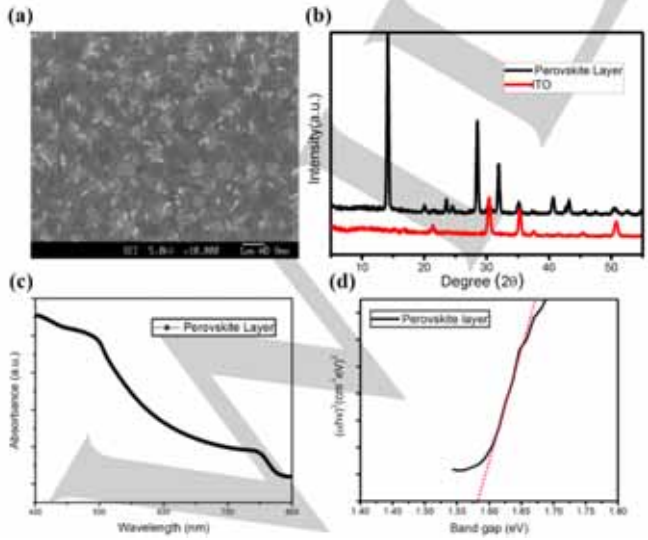

Figure 4. (a) SEM of the perovskite layer surface (new scale bar is required; (b) XRD pattern of prepared perovskite layer; (c) UV-vis absorption spectrum of perovskite layer; (d) band gap of perovskite layer from Tauc plot curve.

The perovskite $FA_yMA_{1-y}PbI_{3-x}Cl_x$ layer was deposited onto the cleaned ITO substrate, pre-coated with the PEDOT: PSS layer using two steps spun cast coating method. Spin-coating were performed at first stage for 15 seconds with 1000 rpm, followed by second step at 5000 rpm for 25 seconds. Then 0.6 mL of toluene was dripped onto perovskite layer and the film were thermally treated at 100 °C for 20 min. The perovskite layer was examined using scanning electron microscopy (SEM) and X-ray diffraction (XRD) analysis are presented in Figure 4a and Figure 4b, respectively. As shown in Figure 2a, SEM image showed the well-developed grain morphology with crystalline platelets of pristine perovskite layer. These platelets were appeared to be hundreds of nanometer in length scale and without any pin holes. Furthermore, we examined the XRD patterns of the deposited perovskite layer, which exhibits five significant characteristic peaks at 43.2°, 41.2°, 31.9°, 28.5°and 14.2°. These peaks can be attributed to the (330), (213), (220) and (110) crystal planes of $FA_yMA_{1-y}PbI_{3-x}Cl_x$, respectively. In XRD analysis no significant peak was observed at 12.6°, indicating absence of free PbI_2 in the perovskite layer. Figure 4c depicts the UV-vis absorption spectra of pristine perovskite film. The corresponding absorption onset value for $FA_yMA_{1-y}PbI_{3-x}Cl_x$ was observed at ~785 nm. The calculated optical band gap from onset absorption value is ~1.58 eV. The calculated band gap was supported by recording the band gap of perovskite layer using Tauc plot as shown Figure 4d.

The schematic structure of inverted p-i-n structured PSCs used in this study with NDI-BTH1 and NDI-BTH2 as ETL is illustrated in Figure 5a. The PSCs device architecture is fabricated as ITO/PEDOT:PSS/ $FA_yMA_{1-y}PbI_{3-x}Cl_x$/ETLs/Ag, where a perovskite light harvester is sandwiched between the bottom poly(3,4-ethylenedioxythiophene):poly(styrene sulphonate) i.e. PEDOT:PSS hole transport layer (HTL), which is deposited on indium tin-oxide (ITO), and the upper n-type semiconductor ETLs. The HTL material extracting the holes from the perovskite layer and collected to the anode (ITO). Whereas, the ETL materials facilitating the efficient electron extraction from perovskite layer and transport to the cathode, silver (Ag) electrode, at the top. Figure 5b provides a schematic illustration of the corresponding energy level diagram for the layers used in this PSCs study. As shown in Figure 5b, LUMO level of NDI-BTH1 and NDI-BTH2 are -4.32 eV and -4.24 eV, respectively, which are close to the conduction band of the perovskite layer. The well-matched energy levels facilitate the favourable electron transfer from the perovskite layer to the Ag electrode *via* ETL layers based on NDI-BTH1 and NDI-BTH2. The HOMO energy levels of NDI-BTH1 (-5.979 eV) and NDI-BTH2 (-5.781 eV) are lower than the valence band of the $FA_yMA_{1-y}PbI_{3-x}Cl_x$ layer, which supports their hole blocking ability towards the Ag electrode. These results implies that NDI-BTH1 and NDI-BTH2 are the promising ETL materials in inverted PSCs.

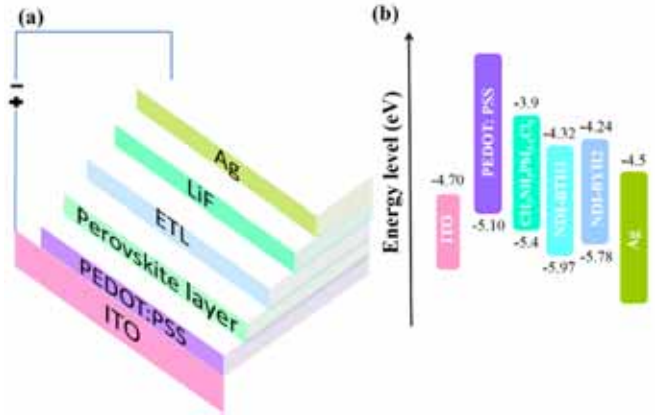

Figure 5. (a) Inverted perovskite solar cell device architecture fabricated in this work; (b) Energy level diagram of each layer used in this work.

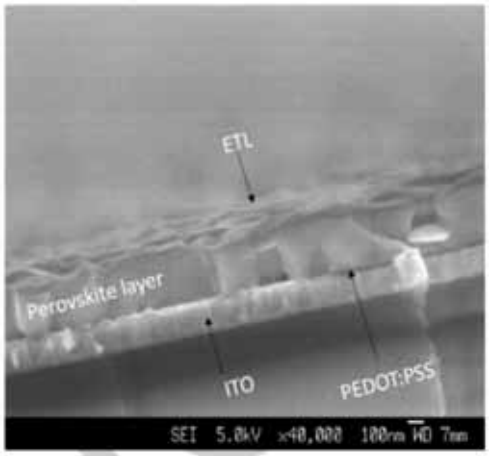

Figure 6. Cross-sectional SEM image of the inverted p-i-n PSCs device: perovskite layer, sandwiched between ITO/PEDOT: PSS and ETL wothout Ag cathode. New scale bar is required

Figure 6 presents the cross-section SEM image of the as-fabricated inverted p-i-n PSCs devce. The thickness of the different layers were clearly observed. The uniform microscale perovskite grains are observed. Such uniform perovskite grains facilitate efficient charge transport and enables more consistance PSCs device performance.

The passivation power toward electron trap centers of NDI-BTH2 is higher than that of NDI-BTH1, which was confirmed by steady-state photoluminescence (PL).Time resolved photoluminescence (TRPL) of $FA_yMA_{1-y}PbI_{3-x}Cl_x$ layer, NDI-BTH1-perovskite bilayer and NDI-BTH2-perovskite bilayer were performed to gain detail insight into the charge extraction process. These results are depicted in Figure 7a and Figure 7b. Upon excitation at 532 nm, peristine perovskite film without ETL exhibits strong photoluminescence at 775 nm. The $FA_yMA_{1-y}PbI_{3-x}Cl_x$ film with the NDI-BTH1 and NDI-BTH2 as the ETL, displayed the quantitative quenching of photoluminescence with blue shift of maximum peak. Interestingly, NDI-BTH1 and NDI-BTH2 showed passivation of electron trap centers. However, NDI-BTH2 has stronger passivation property. Regarding to the maximum peak of bare perovskite layer PL emission, the maximum peak of NDI-BTH2/ perovskite bilayer PL emission showed more blue-shifting than maximum peak of NDI-BTH1/ perovskite bilayer PL emission.[29,30] Thus, it is confirmed that the NDI-BTH1 and NDI-BTH2 are the strong electron acceptors.

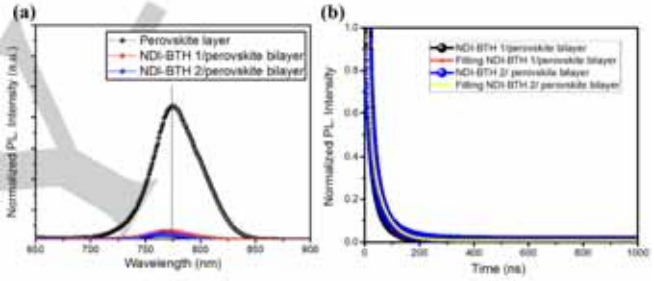

Figure 7. (a) Steady-sate photoluminescence characteristic of perovskite layer, perovskite/NDI-BTH1 bilayer and perovskite/NDI-BTH2 bilayer; (b) Time resolved TRPL of perovskite/NDI-BTH 1 bilayer as well as perovskite/NDI-BTH2 bilayer

Passivation properties were further confirmed by Time-resolved photoluminescence (TRPL) decay experiments of perovskite/ NDI-BTH1 and perovskite/NDI-BTH2 (Figure 7b and Table 4). The PL life-times of perovskite/NDI-BTH1 and perovskite/NDI-BTH2 bilayers were calculated by using an exponential decay with double exponential function 1.

$$Y = Y_0 + A1e^{-x/\tau_1} + A1e^{-x/\tau_2} \qquad (1)$$

Where τ_1 can be ascribed to possible mechanism; non-radiative recombination of charge carriers in perovskite layer and transfer of electrons from perovskite layer to ETL. τ_2 represents the radiative recombination of charge carriers inside perovskite layer.

Table 4. TRPL calculated amplitudes A1, A2 and lifetimes τ_1, τ_2 from Figure 7b

	τ_1 (ns)	A1	τ_2 (ns)	A2
NDI-BTH1	8.86	32668.80	41.35	10385.07
NDI-BTH2	8.62	28188.18	48.15	10615.22

By investigation of τ_1 of each molecule on perovskite layer, it is noted that, the extraction of electrons from perovskite layer by NDI-BTH2 is little faster than NDI-BTH1. The longer life time τ_2 of NDI-BTH2/perovskite bilayer than τ_2 of NDI-BTH1/perovskite bilayer indicated that NDI-BTH2 has stronger passivation property toward electron trap centers than NDI-BTH1.[31,32] In perovskite/NDI-BTH1 and perovskite/NDI-BTH2 bilayers, the life-time τ_1 are 8.86 ns and 8.62 ns, respectively. The PL life-time for these ETL on $FA_yMA_{1-y}PbI_{3-x}Cl_x$ layer were found to significantly decrease comparing that of bare perovskite layer (Table 4). These results revealed faster charge transport and more efficient electron extraction from the perovskite films to NDI-BTH1 and NDI-BTH2 layers. These properties could lead to supress electron/hole recombination and in turn increases the short-circuit current (J_{sc}) and fill-factor (FF). These results clearly demonstrate that NDI-BTH1 and NDI-BTH2 are promising ETL entities comparable with conventional fullerene acceptors such as $PC_{61}BM$ in inverted p-i-n PSCs.

The detailed experiments for fabrication procedure of inverted PSCs are well demonstrated in the experimental section. Under stimulated solar irradiation (AM 1.5, 100 mW cm^{-2}), the current density-voltage (*J-V*) characteristic curves were measured for the inverted PSCs incorporated with NDI-BTH1 and NDI-BTH2 as ETLs. Figure 8a presents the optimal *J-V* curves of the inverted p-i-n PSC device with increasing concentration of the NDI-BTH1 ETLs of 6 mg/mL, 8 mg/mL and 10 mg/mL. The detailed PSCs photovoltaic parameter values are summarized in Table 5. The optimal inverted PSC device with NDI-BTH1 (6 mg/mL) ETL materials yields a power conversion efficiency (PCE) of 11.3%. By applying NDI-BTH1 with concentration of 6 mg/mL, the lower PCE can be associated with the discontinuous ETL thin-film morphology formation over perovskite layer and might lead to charge recombination. As depicted in Figure 8a and Table 5, the PCE of 13.7% is obtained when the PSCs device fabricated with NDI-BTH1 as ETL (8 mg/mL). As shown in Table 5, the other parameters such as an open circuit voltage (V_{oc}) of 0.94 V, a short circuit current (J_{sc}) 21.30 mA/cm^2 and a fill factor (FF) of 60% are obtained from the NDI-BTH1 based devices. The higher J_{sc}, V_{oc} and FF values for PSC device based on NDI-BTH1 ETL are attributed to the higher electron mobility of NDI-BTH1. When the concentration of NDI-BTH1 as ETL reaches 10 mg/mL, each photovoltaic parameter shows considerable decrease with PCE of 10.6%. The decrease in parameters might be due to the higher thickness of aggregated ETL with increase in concentration. The device based on higher thickness of ETL exhibits increased series resistance (R_s) which may lead to lower the FF. The statistical histograms of inverted p-i-n PSCs for 27 individual devices with optimum concentration of NDI-BTH1 are depicted in Figure 8b. The PSCs devices displayed slight variations in PCE. Though photovoltaic performance slightly varied, our devices are reproducible.

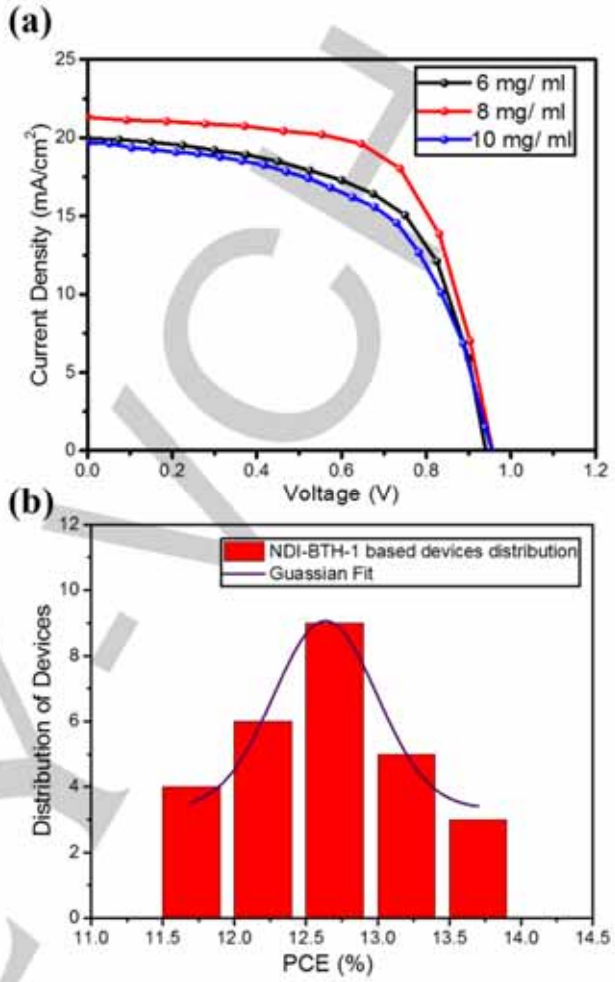

Figure 8. (a) *J-V* curves of PSCs with different concentrations of NDI-BTH1 and (b) distribution of PSCs efficiency for perovskite solar cell with NDI-BTH1 as ETL

Table 5. Photovoltaic parameters of fabricated PSCs with different concentration of NDI-BTH1

	Conc. (mg/mL)	J_{sc} (mA/cm^2)	V_{oc} (V)	FF (%)	PCE (%)
NDI-BTH 1	6	19.95	0.94	60	11.3
	8	21.30	0.96	67	13.7
	10	19.65	0.96	56	10.6

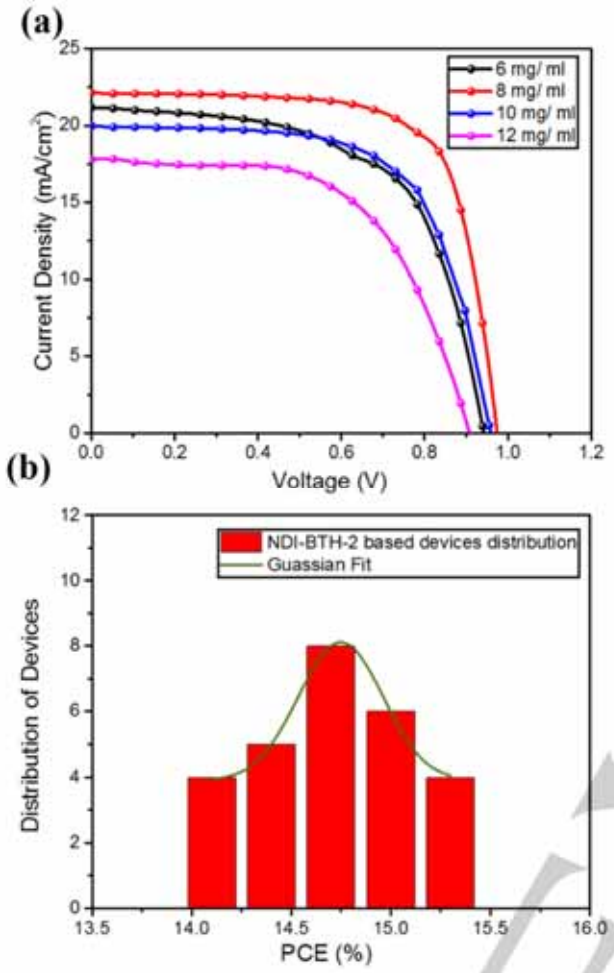

Figure 9. (a) *J-V* curves of PSCs with different concentrations of NDI-BTH2 and (b) distribution of PSCs efficiency for perovskite solar cell with NDI-BTH2 as ETL

Table 6. Photovoltaic parameters of fabricated PSCs with different concentration of **NDI-BTH 2**

	Conc. (mg/mL)	J_{sc} (mA/cm^2)	V_{oc} (V)	FF (%)	PCE (%)
NDI-BTH 2	6	21.17	0.94	60	11.9
	8	22.13	0.98	71	15.4
	10	19.96	0.96	64	12.3
	12	17.85	0.91	58	9.4

Furthermore, the solar cells were fabricated with NDI-BTH2 as ETLs. The current density-voltage (*J-V*) curves of the inverted p-i-n PSC devices based on NDI-BTH2 as an ETL thin film is depicted in Figure 9a. The PSC devices were fabricated an optimized with various concentration of NDI-BTH2 such as 6 mg/mL, 8 mg/mL, 10 mg/mL and 12 mg/mL. The resulted photovoltaic parameters of these PSCs are summerized in Table 6. As shown in Figure 9a and Table 6, the PSC device based on NDI-BTH2 ETL with 6 mg/mL concentration exhibited 11.9% efficiency. When NDI-BTH2 ETL with 8 mg/mL concentartion was employed for PSC device fabrication, the highest efficicncy of 15.4% with short circuit current (J_{sc}) 22.13 mA/cm^2, open circuit voltage (V_{oc}) of 0.98 V, and a fill factor (FF) of 71% was obtained. The higher PCE is associated with the higher electron mobility shown by NDI-BTH2 ETL. Beyond the optimum concentration such as for 10 mg/mL and 12 mg/mL, all of the parameters starts to decrease. When the concentration reaches to 12 mg/mL, considerable decresase in each parameters was observed (Table 6, entry 4) . The explanation for photovoltaic parameters decrease is attributed to the rough thin film formation due to higher concentartion, which might leading to aggregation of the ETL on perovskite thin-film, which in turn results into increase in series resistance and decresae in FF. Figure 9b shows the statistical efficinecy parameters were obtained by fabrication of 27 identical PSC devices employing 8 mg/mL of NDI-BTH2 as ETL. The obtained results suggest though there are small variation in PCEs our device architecture is an efficient one.

The photovoltaic parameters of the optimized PCE device for NDI-BTH2 ETL (8 mg/mL) shows higher PCE of 15.4% compared to 13.7% PCE of PSCs device fabricated using NDI-BTH1 as ETL. The increase in efficiency of PSC with NDI-BTH2 ETL is attributed to (i) its excellent J_{sc} value (22.13 mA/cm^2), (ii) higher elctron mobility as shwon by OFETs, (iii) lower band gap, and (iv) well matched LUMO of NDI-BTH2 with conduction band of perovskite layer. The incerase in sulphur atom leads to more intercation between ETL and I or Pb of perovskite through S-I and S-Pb bonding, which helps in passivation of under-coondinated Pb-atoms. Positively charged under coordinated Pb-atoms act as electron trap centers, which reulted from anti-solvent dripping during the fabrication of perovskite layer. In NDI-BTH2 four benzothiazole moieties and in NDI-BTH1 two benzothiazole subunits are present. The increase in sulphur-atoms yields lower the LUMO level of NDI-BTH2 and matches with the conduction band of $FA_yMA_{1-y}PbI_{3-x}Cl_x$. This might lead to enhance charge extraction efficiency from perovskite layer and transportation to the Ag cathod is higher. We presume that these parameters are involved to enhance the PCE of PSCs devices with NDI-BTH2 ETL. We also investigated the *I-V* curves of the inverted PSCs devices with the NDI-BTH1 and NDI-BTH2 ETLs in the dark as depicted in Figure S17. The dark current curves clearly display that the leakage current of the NDI-BTH2 based device is slightly lower than that of the NDI-BTH1 PSC device. In addition, the rectifying behaviour significally appeared stronger in NDI-BTH2 based devices than NDI-BTH1 based devices. We presume that the NDI-BTH2 ETL has higher coverage on the perovskite thin-film compared with the NDI-BTH1 ETL, which ultimately prevent the leakage of current.

To better understand the behavior of the NDI-BTH1 and NDI-BTH2 ETLs materials on the interfacial recombination at the interface between the ETL and the $FA_yMA_{1-y}PbI_{3-x}Cl_x$ in the performance of PSCs devices, the electrochemical impedance spectroscopy (EIS) method was applied. The EIS is the effective techniques to get an in-depth idea about interfacial behavior in

PSCs. The EIS properties are investigated in the dark under forward biases. The characteristic Nyquist plots of PSCs device with NDI-BTH1 and NDI-BTH2 ETLs are depicted in Figure 10, which gives the information about the photogenerated hole/electron pairs and the charge transfer resistance.[33] As shown in Figure 10, for PSCs with NDI-BTH1 and NDI-BTH2 ETLs exhibits two semicircles with higher and lower frequency regions. These semicircles are related to the two different charge transfer properties. At higher frequency in both spectra an arc is observed, which represents the charge transfer resistance. In fact, the charge transfer resistance of NDI-BTH2-based devices is slightly lower than that of NDI-BTH1-based devices. In addition the charge recombination resistance, which is represented by semicircle curve at lower frequency, is significantly higher in NDI-BTH2-based devices than NDI-BTH1-based devices. In the Nyquist plot, the lower frequency is for the charge transfer through $FA_yMA_{1-y}PbI_{3-x}Cl_x$ /ETL interface contact and the higher frequency is for the charge transport associated in the identical region.[34,35] At increasing higher forward bias the electron transfer from $FA_yMA_{1-y}PbI_{3-x}Cl_x$ to ETL improves and the decrease in the charge recombination resistance (R_{rec}) at the interface of perovskite and ETL was observed.

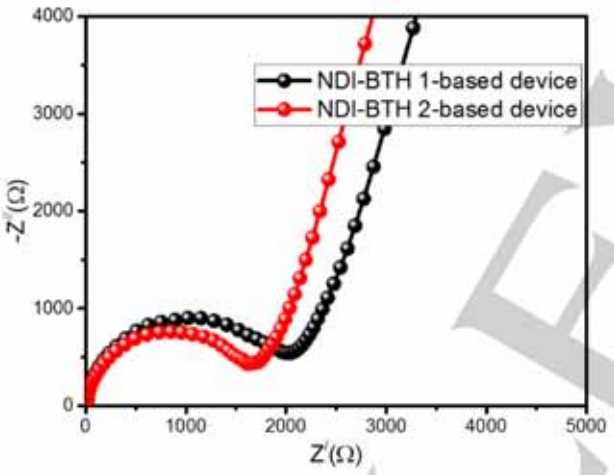

Figure 10. Electrochemical impedance spectroscopy characterization of PSCs devices with NDI-BTH1 and NDI-BTH2 ETLs.

Conclusions

In summary, we have reported the synthesis and semiconducting properties of novel benzothiazole-NDI based small molecules NDI-BTH1 and NDI-BTH2. The NDI-BTH1 exhibits n-type semiconducting behavior with electron mobility up to 14.00 x 10^{-5} cm^2/Vs after annealing. Whereas, at 140 °C, NDI-BTH2 displays ambipolar-type semiconductor properties with μ_e (8.64 x 10^{-4} cm^2/Vs) and μ_h (1.68 x 10^{-4} cm^2/Vs) mobilities. Both the chromophores serve as ETL in inverted p-i-n PSCs. Our work suggests that the PSCs with NDI-BTH2 as ETL demonstrated the highest PCE of 15.4%. On the other hand, the NDI-BTH1 with two benzothiazole subunits displayed lower efficiency of 13.7%, attributed to lower electron mobility. The higher efficiency exhibited by NDI-BTH2 is attributed to an efficient charge transport and reduction in charge recombination as the higher forward bias increases. This work demonstrates the promising utility of core modified NDI with benzothiazole acceptor to improve the PSCs device performance.

Experimental Section

Materials and Methods

Reagents and solvents used in this work are 1,4,5,8-naphthalenetetracarboxylic dianhydride (NDA), 1,3-dibromo-5,5-dimethyl hydantoin (DBH), n-octylamine, 2-tributylstannylthiophene, *bis*-(triphenylphosphine) palladium (II) dichloride, phosphorus oxychloride, *N,N*-dimethylformamide, triethyl phosphite and 2-aminothiophenol, malononitrile, acetic acid. These chemicals were purchased from Alfa Aesar (Mumbai), TCI (Chennai) and Sigma-Aldrich (Bengaluru) Pvt. Ltd., India. Solvents were purchased from Finar (Ahmadabad/Mumbai), Spectrochem (Mumbai) and Merck (Mumbai), India and they were further purified by the standard purification methods. ^{1}H and ^{13}C NMR spectra were recorded as stated in experimental procedure at 300, 400 or 500 and 75, 100 or 125 MHz respectively by using tetramethylsilane internal standard. The chemical shift (δ) of protons were represented in part per million (ppm) and coupling constant (*J*) was reported in Hertz (Hz). The splitting pattern was denoted as singlet (s), doublet (d), triplet (t) and multiplets (m). Furthermore, FT-IR spectra were recorded on Thermo Nicolet Nexus 670 instrument and Mass spectra measured on Schimadzu Biotech Axima MALDI–TOF Mass Spectrometer. Moreover, UV-vis spectra was recorded in a UV 1800 Schimadzu spectrophotometer at room temperature in dichloromethane solvent (1 X 10^{-5} M). Cyclic voltammeter measurements were also carried out with AUTOLAB PGSTAT 302 N at a scan rate 50 mVs^{-1}. The solvent used for measurement was DCM with $TBAPF_6$ (0.1 M) as electrolyte.

Synthetic procedure for compound 2[36]

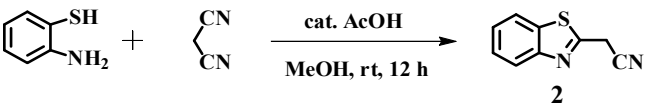

2

In 50 mL clean oven dried round bottom flask, 2-aminothiophenol (1.0 g, 0.0079 mol) and malononitrile (0.63 g, 0.0095 mol) in 25 mL methanol solvent has taken and stirred at room temperature for 5 minutes followed by slow addition of catalytic acetic acid (1 mL). After the addition, reaction mixture was further stirred for 10 h at room temperature. The completion of reaction was monitored by TLC and then solvent was evaporated, the obtained crude solid was washed with methanol to afford orange solid in 92.51 % reaction yield (1.544 g). ^{1}H NMR ($CDCl_3$, 400 MHz) δ ppm = 8.05 (d, 1H, *J* = 8.19 Hz), 7.90 (d, 1H, *J* = 8.55 Hz), 7.54 – 7.52 (m, 1H), 7.46 – 7.42 (m, 1H), 4.24 (s, 2H), ^{13}C NMR ($CDCl_3$, 100 MHz) 158.18, 152.78, 135.40, 126.68, 125.93, 123.35, 121.69, 114.83, 23.18.

Synthetic procedure for compound 3[37]

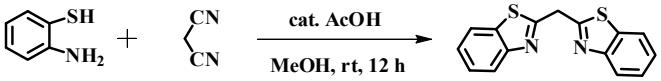

3

In 50 mL clean oven dried round bottom flask has charged with 2-aminothiophenol (2.66 g, 0.0212 mol) and malononitrile (0.26 g 0.0039 mol) in 25 mL methanol solvent and stirred at room temperature for 5 minutes, then the acetic acid being used as catalyst was added slowly (1mL). After the addition, reaction mixture was kept stirring for 15 h at refluxed temperature. The completion of reaction was monitored by TLC. Then, reaction mixture was cooled to room temperature; solvent evaporated and obtained solid was washed with methanol. This crude product was further purified by column chromatography by using hexane and ethyl acetate (8:2 v/v) eluent to afford greyish solid in 65 % reaction yield (3.89 g). ^{1}H NMR ($CDCl_3$, 400 MHz) δ ppm = 8.05 – 8.03 (d, 2H, *J* = 8.06 Hz), 7.85 – 7.82 (d, 2H, *J* = 8.06 Hz), 7.50 – 7.46 (m, 2H), 7.39 – 7.35 (m, 2H), 4.94 (s, 2H).; ^{13}C NMR ($CDCl_3$, 100 MHz) δ ppm = 165.56, 153.00, 135.74, 128.28, 126.18, 125.29, 123.10, 121.58, 38.85.

Synthesis of (2E,2'E)-3,3'-(5,5'-(2,7-dioctyl-1,3,6,8-tetraoxo-1,2,3,6,7,8-hexahydrobenzo[lmn][3,8]phenanthroline-4,9-diyl)bis(thiophene-5,2-diyl))bis(2-(benzo[d]thiazol-2-yl)acry lonitrile) **[NDI-BTH 1]**

In 50 mL round bottom flask, 5,5'-(2,7-dioctyl-1,3,6,8-tetraoxo-1,2,3,6,7,8-hexahydrobenzo[lmn][3,8]phenanthroline-4,9-diyl)bis(thiophene-2-carbal dehyde) **1** (150 mg, 0.2113 mmol) 15 mL dry dichloromethane and acetonitrile (1:1), and 2-(benzo[d]thiazol-2-yl)acetonitrile **2** (80.98 mg, 0.4648 mmol) have taken. To this mixture, piperidine was added in catalytic amount and the reaction mixture was stirred at room temperature for 15 minutes followed by refluxing the mixture at 70 °C for 12 h. Completion of reaction was monitored by TLC. Reaction mixture was cooled, solvent evaporated by rotary evaporator and the crude product was purified by column chromatography on silica gel (100–200 mesh) using dichloromethane and hexane (1:1) as an eluent to afford black solid **NDI-BTH 1** (140 mg, 64.76 %). M.P. 214-216 °C (open capillary, uncorrected); FT-IR (γ, cm^{-1}, KBr) 2921, 2851, 2213, 1705, 1665, 1572, 1428, 1376, 1310, 1251, 1185, 1086, 973, 935, 799, 756, 722, 586, 546.; ^{1}H NMR ($CDCl_3$, 500 MHz) δ ppm 8.77 (s, 2H), 8.45 (s, 2H), 8.08 – 8.06 (d, 2H, *J* = 8.08 Hz), 7.92 – 7.89 (m, 4H), 7.56 – 7.52 (t, 2H, *J* = 7.17 Hz), 7.46 – 7.42 (d, 2H, *J* = 7.17 Hz), 7.37 – 7.36 (d, 2H, *J* = 3.96 Hz), 4.13 – 4.10 (t, 4H, J = 7.47 Hz),1.72 – 1.66 (m, 4H), 1.38 – 1.25 (m, 20H), 0.86 – 0.84 (t, 6H, *J* = 6.17 Hz). ;^{13}C NMR ($CDCl_3$, 100 MHz) δ ppm = 161.61, 153.70, 148.17, 138.86, 138.24, 135.77, 135.09, 129.20, 127.68, 127.00, 125.92, 124.07, 123.42, 121.70, 116.61, 102.77, 41.37, 31.75, 29.68, 29.16, 27.97, 27.04, 22.59, 14.06.; MALDI-TOF calculated mass for $C_{58}H_{50}N_6O_4S_4$. 1023.32. Found: 1023.18 [M]$^+$.

Synthesis of 4,9-bis(5-(2,2-bis(benzo[d]thiazol-2-yl)vinyl)thiophen-2-yl)-2,7-dioctylbenzo [lmn][3,8]phenanthroline-1,3,6,8(2H,7H)-tetraone **[NDI-BTH 2]**

Dry dichloromethane and acetonitrile solvents (1:1) was taken in 50 mL oven dried round bottom flask, to this solvent mixture compound 5,5'-(2,7-dioctyl-1,3,6,8-tetraoxo-1,2,3,6,7,8-hexahydrobenzo[lmn][3,8]phenanthro line-4,9-diyl)bis- (thiophene-2-carbaldehyde) **1**[27] (150 mg, 0.2113 mmol and bis(benzo[d]thiazol-2-yl)methane **3** (282.38 mg, 0.4648 mmol) were added. Piperidine was added in a catalytic amount and the resulting mixture was stirred at room temperature for 15 minutes followed by refluxed at 70 °C for 12 h. After completion of reaction, mixture was cooled to room temperature and solvent was evaporated by rotary evaporator. The crude product was purified by column chromatography on silica gel (100–200 mesh) dichloromethane: hexane (1:1) as an eluent to afford green solid NDI-BTH 2 (190 mg, 72.57 %). M.P. 240-242 °C (open capillary, uncorrected); FT-IR (γ, cm^{-1}, KBr) 3447, 3056, 2921, 2851, 1703, 1664, 1566, 1435, 1376, 1311, 1246, 1184, 1093, 1046, 919, 868, 792, 755, 723, 546, 429.; ^{1}H NMR ($CDCl_3$, 400 MHz) δ ppm = 8.54 (s, 2H), 8.22 (s, 2H), 8.16 – 8.14 (d, 2H, *J* = 8.07 Hz), 8.02 – 8.00 (d, 2H, *J* = 8.19 Hz), 7.95 – 7.93 (d, 2H, J = 7.82 Hz), 7.82 – 7.80 (d, 2H, *J* = 7.94 Hz), 7.49 – 7.34 (m, 10H), 7.13 – 7.12 (d, 2H, *J* = 3.79 Hz), 3.98 – 3.94 (t, 4H, *J* = 7.21 Hz), 1.60 – 1.54 (m, 4H), 1.30 – 1.25 (m, 20H), 0.88 – 0.84 (t, 6H, *J* = 6.48 Hz).; ^{13}C NMR ($CDCl_3$, 100 MHz) δ ppm = 167.31, 162.63, 162.06, 161.82, 154.04, 153.43, 146.47, 140.39, 139.51, 137.25, 136.24, 135.51, 135.21, 131.45, 128.50, 127.64, 126.81, 126.10, 125.69, 125.54, 125.35, 124.26, 123.58, 122.15, 121.69, 41.41, 32.07, 29.99, 29.49, 28.19, 27.35, 22.92, 14.39.; MALDI-TOF calculated mass for $C_{70}H_{58}N_6O_4S_6$. 1239.64. Found: 1239.19 [M]$^+$.

Computational calculation method

The molecules NDI-BTH-1 and NDI-BTH-2 were first structurally optimized and vibrational frequencies analyzed using the hybrid B3LYP density functional with a 6-31G(d) basis set. One hundred (100) singlet-to-singlet excitation energies of these molecules were then computed using linear response time-dependent density functional theory (TD-DFT)[28a,28b] and the same B3LYP functional with a larger, more diffuse 6-31+G(d) basis set with tighter screening thresholds of 10^{-16} for integrals. Theoretical UV-visible spectrum of NDI-BTH-1 and NDI-BTH-2 were then approximated assuming a Lorentzian band shape about each excitation vertical peak, and are shown in Figure S15 and S16. Details of the dominant peaks and frontier molecular orbitals are provided in Tables S1, S2 and S3 (SI). The extent of charge transfer in a particular excited state was determined using a spatial overlap metric from Peach *et al.*, also known as a lambda diagnostic.[28c] All calculations were carried out using Q-Chem 5.0.[28d]

OFET Device Fabrication Method

The charge transport property of NDI-BTH 1 and NDI-BTH 2 were investigated by the bottom-gate top-contact (BGTC) organic thin-film field effect transistors (OTFTs) with the *n*-octadecyltrimethoxylsilane (OTS) modified SiO_2 (300nm, C_i = 11 nF/cm^2) as dielectric layer, the highly n-doped silicon wafer as gate electrode and the thermally evaporated gold as source/drain electrodes. The thin film was obtained by spin-coating.

Perovskite Device Fabrication Method

The fabrication started by spin coated of PEDOT: PSS on ITO at 6000 rpm for 1 minute. After Heat treatment PEDOT: PSS at 15 minutes at 135 °C, perovskite layer (PbI_2 1.26 M, $PbCl_2$ 0.14 M, MAI 1.08 M and FAI 0.27 M in DMSO, GBL (3:7, v: v)) was spun cast on PEDOT: PSS at two steps. The first step at 1000 rpm for 15 s, the followed by second step which is proceeded at 5000 rpm, after 25 s of start of the second step, 600 ml of toluene is dripped onto perovskite layer. Then the as prepared perovskite layer is heat treated at 100 °C for 20 minutes. NDI-BTH 1 and NDI-BTH 2 solutions in dichlorobenzene are spun cast on perovskite layer at 2200 rpm for 1 minute, followed by heat treated at 95 °C for 10 minutes. The final step of PSCs device fabrication was completed by evaporation of 100 nm of Ag electrode.[38]

Device Characterization

The perovskite layer was investigated by powder XRD equipped with CuKα radiation (λ = 0.15418 nm operated at 40 kV and 30 mA). The surface morphology and cross section of perovskite film were investigated by SEM (JEOL, JSM 6360 at 5 KV). The optical properties of the perovskite layer were characterized by UV–vis spectroscopy (UV–vis–NIR, Lambda 900, Perkin Elmer). The PL characteristics were measured by Cary Eclipse

Fluorescence Spectrophotometer (Agilent Technologies). TRPL was measured by PicoHarp 300, PicoQuant. Contact angle of each ETL was measured by contact angle equipment, Data Physics, OCA 15 Pro. Electrochemical Impedance Spectroscopy (EIS) was analysed on a CHI 660 C Electrochemical Workstation The current density–voltage (*J–V*) curves of solar cells were measured using Keithley 2400 source meter under a simulated AM1.5 G illumination (100 mW cm^{-2}) by a Xenon-lamp-based solar simulator (Abet Technologies, USA). The light intensity was calibrated using a Si-reference cell certified by the National Renewable Energy Laboratory.

Electrochemical impedance spectroscopy

Acknowledgements

S.V.B. (IICT) is grateful for the financial support from The Director, CSIR-IICT, Hyderabad, India. IICT Communication Number IICT/Pubs./2019/----------. S.V.B. (GU) acknowledges University Grants Commission-Faculty Recharge Program (India). D.B.S. acknowledges SRF fellowship from UGC, New Delhi. Q.Z. acknowledges financial support from AcRF Tier 1 (RG 111/17, RG 2/17, RG 114/16, RG 8/16) and Tier 2 (MOE 2017-T2-1-021 and MOE 2018-T2-1-070), Singapore. QZ also thanks the support (sklssm2019036) from State Key Laboratory of Supramolecular Structure and Materials, Jilin University, Changchun, P. R. China.

‡**Present Address:** Department of Chemistry, Indrashil University, Kadi, Mehsana-382740, Gujarat, India

Conflict of interest

The authors declare no conflict of interest

Keywords: electron transport • naphthalenediimides • OFETs• perovskite • solar cells

1 a) P. F. Van Hutten, V. V. Krasnikov, G. Hadziioannou, *Acc. Chem. Res.* **1999**, *32*, 257-265; b) J. Zaumesil, H. Sirringhaus, *Chem. Rev.* **2007**, *107*, 1296-1323; c) H. Sirringhaus, *Adv. Mater.* **2014**, *26*, 1319-1335; d) Y. P. Zhang, F. J. Zhang, D. Z. Huang, X. K. Gao, C. A. Di, D. B. Zhu, *Nat. Commun*. **2015**, *6*, 6269; e) J. Y. Oh, S. Rondeau-Gagné, Y. C. Chiu, A. Chortos, F. Lissel, G.-J. N. Wang, B. C. Schroeder, T. Kurosawa, J. Lopez, T. Katsumata, J. Xu, C. X. Zhu, X. D. Gu, W.-G. Bae, Y. Kim, L. Jin, J. W. Chung, J. B.-H. Tok, Z. N. Bao, *Nature* **2016**, *539*, 411-415; (f) J. Li, S. Chen, Z. Wang, Q. Zhang, *Chem. Record*, **2016**, *16*, 1518-1530; (g) Y. Huang, Z. Wang, Z. Chen, Q. Zhang, *Angew. Chem Int. Ed.* **2019**, *58*, 9696-9711

2 a) W. Liu, Y. Zhou, Y. Ma, Y. Cao, J. Wang, J. Pei, *Org. Lett*. **2007**, *9*, 4187-4190; b) I. Osaka, T. Abe, S. Shinamura, E. Miyazaki, K. Takimiya, *J. Am. Chem. Soc.* **2010**, *132*, 5000-5001; c) T. Lei, Y. Cao, Y. Fan, C. Liu, S. Yuan, J. Pei, *J. Am. Chem. Soc.* **2011**, *133*, 6099-6101; d) K. Kuribara, H. Wang, N. Uchiyama, K. Fukuda, T. Yokota, U. Zschieschang, C. Jaye, D. Fischer, H. Klauk, T. Yamamoto, K. Takimiya, M. Ikeda, H. Kuwabara, T. Sekitani, Y. Loo, T. Someya, *Nat. Commun*. **2012**, *3*, 723; e) W. Jiang, Y. Li, Z. Wang, *Chem. Soc. Rev.* **2013**, *42*, 6113; f) K. Takimiya, S. Shinamura, I. Osaka, E. Miyazaki, *Adv. Mater.* **2011**, *23*, 4347; (g) P. Gu, Z. Wang, G. Liu, H. Yao, Z. Wang, Y. Li, J. Zhu, S. Li, Q. Zhang, *Chem. Mater*. **2017**, *29*, 4172-4175; (h) J. Zhang, J. Jin, H. Xu, Q. Zhang, W. Huang, *J. Mater. Chem. C*, **2018**, *6*, 3485 – 3498

3 L. Chua, J. Zaumseil, J. Chang, E. Ou, P. Ho, H. Sirringhaus, R. Friend, *Nature* **2005**, *434*, 194

4 H. Li, B. C. Tee, J. J. Cha, Y. Cui, J. W. Chung, S. Y. Lee, Z. Bao, *J. Am. Chem. Soc*. **2012**, *134*, 2760-2765.

5 L. Chua, J. Zaumesil, J. Chang, E. C.-W. Ou, P. K.-H. Ho, H. Sirringhaus, R. H. Friend, *Nature* **2005**, *434*, 194-199.

6 a) M. Shkunov, R. Simms, M. Heeney, S. Tierney, I. McCulloch, *Adv. Mater.* **2005**, *17*, 2608; b) H. Usta, A. Facchetti, T. J. Marks, *J. Am. Chem. Soc*. **2008**, *130*, 8580-8581; c) L. Bürgi, M. Turbiez, R. Pfeiffer, F. Bienewald, H.-J. Kirner, C. Winnewisser, *Adv. Mater.* **2008**, *20*, 2217–2224; d) R. Capelli, S. Tofanin, G. Generali, H. Usta, A. Facchetti, M. Muccini, *Nat. Mater.* **2010**, *9*, 496-503; e) C. Wang, H. Dong, W. Hu, Y. Liu, D. Zhu, *Chem. Rev.* **2012**, *112*, 2208-2267; f) Y. Zhao, Y. Guo, Y. Liu, *Adv. Mater.* **2013**, *25*, 5372-5391; g) S. Bisri, C. Piliego, J. Gao, M. Loi, *Adv. Mater.* **2014**, *26*, 1176–1199; h) X. Chen , G. Zhang, H. Luo, Y. Li , Z. Liu, D. Zhang, *J. Mater. Chem. C* **2014**, *2*, 2869-2876; i) H. Yoo, M. Ghittorelli, D.-K. Lee, E. C. P. Smits, G. H. Gelinck, H. Ahn, H.-K. Lee, F. Torricelli, J.-J. Kim, *Sci. Rep*. **2017**, *7*, 5015.

7 A. Kojima, K. Teshima, Y. Sharai, T. Miyasaka, J. Am. Chem. Soc. **2009**, *131*, 6050-6051

8 a) M. Saliba, J.-P. Correa-Baena, C. M. Wolff, M. Stolterfoht, N. Phung, S. Al-brecht, D. Neher, A Abate, *Chem. Mater.* **2018**, *30*, 4193-4201; b) W. S. Yang, B.-W. Park, E. H. Jung, N. J. Jeon, Y. C. Kim, E. U. Lee, S. S. Shin, J. Seo, E. K. Kim, J. H. Noh, S. I. Seok, *Science* **2017**, *356*, 1376-1379; c) S.-K. Jumg, D. S. Lee, M. H. Ann, S. H. Im, J. H. Kim, O-P. Kwon, ChemSusChem, 2018, 11, 3882-3892; d) X. Li, D. Bi, C. Yi et al., *Science* **2016**, *353*, 58–62.

9 a) K. Aitola, K. Domanski, J.-P. Correa-Baena, K. Sveinbjörnson, M. Saliba, A. Abate, M. Grätzel, E. Kauppinen, E. M. J. Johansson, W. Tress, A. Hagfeldt, G. Boschloo, *Adv. Mater.* **2017**, *29*, 1606398; b) H. Tan, A. Jain, O. Voznyy, X. Lan, F. P. García de Arquer, J. Z. Fan, R. Quintero-Bermudez, M. Yuan, B. Zhang, Y. Zhao, F. Fan, P. Li, L. N. Quan, Y. Zhao, Z.-H. Lu, Z. Yang, S. Hoogland, E. H., *Science* **2017**, *335*,722-726.

10 I. Hussain, H. P. Tran, J. Jaksik, J. Moore, N. Islam, M. J. Uddin, *Emergent Mater.* **2018**, *1*, 133–154

11 a) Y. Fang, C. Bi, D. Wang, J. Huang, *ACS Energy Lett.* **2017**, *2*, 782-794; b) R. Sandoval-Torrientes, J. Pascual, I. García-Benito, S. Collavini, I. Kosta, R. Tena-Zaera, N. Martín, J. L.Delgado, *ChemSusChem* **2017**, *10*, 2023-2029

12 W. Qiu, M. Buffière, G. Brammertz, U. W. Paetzold, L. Froyen, P. Heremans, D. Cheyns, *Org. Electronics* **2015**, *26*, 30-35.

13 A. Anctil, C. W. Babbitt, R. P. Raffaelle, B. J. Landi, *Environ. Sci. Technol.* **2011**, *45*, 2353-2359.

14 a) W. Wang, J. Yuan, G. Shi, X. Zhu, S. Shi, Z. Liu, L. Han, H. Q. Wang, W. Ma, *ACS Appl. Mater. Interfaces* **2015**, *7*, 3994-3999; b) A. A. Said, J. Xie, Y. Wang, Z. Wang, Y. Zhou, K. Zhao, W.-B. Gao, T. Michinobu, Q. Zhang,.*Small* **2018**, 1803339; c) Y. Liu, L. Zhang, H. Lee, H. W. Wang, A. Santala, F. Liu, Y. Diao, A. L. Briseno, T. P. Russell, *Adv. Energy Mater.* **2015**, *5*, 1500195; d) Sun, Z. Wu, H. L. Yip, H. Zhang, X. F. Jiang, Q. Xue, Z. Hu, Y. Shen, M. Wang, F. Huang, Y. Cao, *Adv. Energy Mater.* **2016**, *6*, 1501534; e) S. Shao, Z. Chen, H. H. Fang, G. H. Brink, D. Bartesaghi, S. Adjokatse, L. J. A. Koster, B. J. Kooi, A. Facchettib, M. A. Loi, *J. Mater. Chem. A* **2016**, 4, 2419-2426; f) S. Y. Liu, W. Q. Liu, C. X. Yuan, A. G. Zhong, D. Han, B. Wang, M. N. Shah, M. M. Shi, H. Chen, *Dyes and Pigments* **2016**, *134*, 139-147; g) X. Xu, W. Xing, Y. Chen, F. Liu, X. Wu, T. Dong, P. Ye , Z. Liu, H. Huang, *Synthetic Metals* **2017**, *231*, 19–24; h) H. Liu, Z. Zhang, M. Huang, B. Zhao, J. Zhang, S. Tan, *Synthetic Metals* **2017**, *227*, 122–130; i)L. M.J. Moore, M. B. Norman, A. R. Benasco, J. M. Richardson, S. E. Morgan, *Synthetic Metals* **2018**, *237*, 56–64; j) A. A. Said, J. Xie, Q. Zhang, *Small*, **2019**, 1900854; (k) A. A. Said, J. Xie, Y. Wang, Z. Wang, Y. Zhou, K. Zhao, W. Gao, T. Michinobu, Q. Zhang, *Small*, **2019**, *15*, 1803339

15 M. Zhang, X. Zhan, *Adv. Energy Mater.* **2019**, *9*, 1900860.

16 a) P. Gu, N. Wang, A. Wu, Z. Wang, M. Tian, Z. Fu, X. Sun, Q. Zhang, *Chem. Asian J.* **2016**, *11*, 2135-2138. b) P. Gu, N. Wang, C. Wang, Y. Zhou, G. Long, M. Tian, W. Chen, X. Sun, M. G. Kanatzidis, Q. Zhang, *J. Mater. Chem. A* **2017**, *5*, 7339-7344; (c) P. Gu, Y. Zhao, J. He, J. Zhang, C. Wang, Q. Xu, J. Lu, X. Sun, Q. Zhang, *J. Org. Chem.* **2015**, *80*, 3030-3035; (d) J. Li, P. Li, J. Wu, J. Gao, W. Xiong, G. Zhang, Y. Zhao, Q. Zhang, *J. Org. Chem*. **2014**, *79*, 4438-45; (e) P. Gu, Z. Wang, Q. Zhang, *J. Mater. Chem. B,* **2016**, *4*, 7060 – 7074.

17 a) Z. Zhu, D. Zhao, C. C. Chueh, X. Shi, Z. Li, A. Jen, *Joule* **2018**, *2*, 168-183; b) D. Zhao, Z. Zhu, M. Y. Kuo, C. C. Chueh, A. Jen, *Angew. Chem. Int. Ed*. **2016**, *55*, 8999–9003.

18 a) J. L. Wu, W. K. Huang, Y. C. Chang, B. C. Tsai, Y. C. Hsiao, C. Y. Chang, C. Ti. Chen, C. T. Chen, *J. Mater. Chem. A* **2017**, *5*, 12811-12821; b) K. Jiang, F. Wu, H. Yu, Y. Yao, G. Zhang, L. Zhu, H. Yan, *J. Mater. Chem. A* **2018**, *6*, 16868-16873; c) Q. Gup, Y. Xu, B. Xiao, B. Zhang, E. Zhou, F. Wang, Y. Bai, T. Hayat, A. Alsaedi, Z. Tan, *ACS Appl. Mater. Interfaces* **2017**, *9,* 10983-10991; d) P. Karuppuswamy, H.-C. Chen, P.-C. Wang, C.-P. Hsu, K.-T. Wong, C.-W. Chu, *ChemSusChem* **2018**, *11*, 415-423.

19 R. Wang, J. Qiao, B. He, X. Tang, F. Wu, L. Zhu, *J. Mater. Chem. C* **2018**, *6*, 8429-8434.

20 N. Wang, K. Zhao, T. Ding, W. Liu, A. S. Ahmed, Z. Wang, M. Tian, X. W. Sun, Q. Zhang, *Adv. Energy Mater.* **2017**, *7*, 1700522.

21 Z. Zhu, J. Q., Xu, C.-C. Chueh, H. Liu, Z. Li, X. Li, H. Chen, A. K.-Y. Jen, *Adv. Mater.* **2016**, *28*, 10786-10793.

22 a) Z. Zhu, C.-C. Chueh, G. Zhang, F. Huang, H. Yan, A. K-Y. Jen, *ChemSusChem* **2016**, *9*, 2586-2591; b) C. Sun, Z. Wu, H.-L. Yip, H. Zhang, X.-F. Jiang, Q. Xue, Z. Hu, Z. Hu, Y. Shen, M. Wang, F. Huang, Y. Cao, *Adv. Energy Mater.* **2016**, *6*, 1501534; c) J. H. Heo, S.-C. Lee, S.-K. Jung, O. P. Kwon, S. H. Im, *J. Mater. Chem. A* **2017**, *5*, 20615-20622; d) S.-K. Jung, J. H. Heo, D. W. Lee, S.-C. Lee, S.-H. Lee, W. Yoon, H. Yun, S. H. Im, J. H. Kim, O.-P. Kwon, *Adv. Funct. Mater.* **2018**, 1800346; e) S.-K. Jung, J. H. Heo, D. W. Lee, S.-H. Lee, S.-C. Lee, W. Yoon, H. Yun, D. Kim, J. H. Kim, S. H. Im, O.-P. Kwon *ChemSusChem* **2019**, *12*, 224-230; f) H. I. Kim, M.-J. Kim, K. Choi, C. Lim, Y.-H. Kim, S.-K. Kwon, T. Park, *Adv. Energy Mater.* **2018**, *8*, 1702872; (similar to reference 27)

23 a) X. Gao, C. Di, Y. Hu, X. Yang, H. fan, F. Zhang, Y. Liu, H. Li, D. Zhu, *J. Am. Chem. Soc.* **2010**, *132*, 3697-3699; b) Y. Zhao, C. Di, X. Gao, Y. Hu, L. Zhang, Y. Liu, J. Wang, W. Hu, D. Zhu, *Adv. Mater.* **2011**, *23*, 2448-2453; c) Y. Hu, X. Gao, C. Di, X. Yang, F. Zhang, Y. Liu, H. Li, D. Zhu, *Chem. Mater.* **2011**, *23*, 1204-1215.

24 T. Zhu, L. Jiang, Y. Li, Z. Xie, Z. Li, L. Lv, H. Chen, Z. Zhao, L. Jiang, B. tang, H. Huang, *Angew. Chem. Int., Ed.* **2019**, *58*, 5044-5048.

25 M. Al Kobaisi, S. V. Bhosale, K. Latham, A. M. Raynor, S. V. Bhosale, *Chem. Rev*. **2016**, *116*, 11685-11796.

26 a) M. Saliba, S. Orlandi, T. Matsui, S. Aghazada, M. Cavazzini, J.-P. Correa-Baena, P. Gao, R. Scopelliti, E. Mosconi, K.-H. Dahmen, F. De Angelis, A. Abate, A. Hagfeldt, G. Pozzi, M. Graetzel, M. K. Nazeeruddin, *Nat. Energy* **2016**, *1*, 15017; b) N. K. Noel, A. Abate, S. D. Stranks, E. S. Parrott, V. M. Burlakov, A. Goriely, H. J. Snaith, *ACS Nano* **2014**, *8*, 9815-9821.

27 D. B. Shaikh, A. A. Said, R. S. Bhosale,W. Chen,S. V. Bhosale, A. L. Puyad,S. V. Bhosale, Q. Zhang, *Asian J. Org. Chem.* **2018**, *7*, 2294-2301.

28 a) E. Runge, E. K. U. Gross, *Phys. Rev. Lett.* **1984**, *52*, 997-1000; b) M. E. Casida, in *Recent Advances in Density Functional Methods, Part I;* Chong, D.P., Ed.; World Scientific: Singapore, **1995**; pp 155-193; (c) M. J. Peach, P. Benfield, T. Helgaker, D. J. Tozer, *J. Chem. Phys.* **2008**, *128*, 044118; d) Y. Shao, et al., *Mol. Phys.* **2015**, *113*, 184-215.

29 Y. H. Shao,; Z. G. Xiao, C. Bi, Y. B. Yuan, J. S. Huang, *Nat. Commun.* **2014**, *5*, 5784.

30 C. Sun, Z. H. Wu, H. L. Yip, H. Zhang, X. F. Jiang, Q. F. Xue, Z. C. Hu, Z. H.Hu, Y. Shen, M. K. Wang, F. Huang, Y. Cao, *Adv. Energy Mater.* **2016**, *6*, 1501534.

31 Y. Xing, C. Sun, H. L. Yip, G. C. Bazan, F. Huang, Y. Cao, *Nano Energy* **2016**, *26*, 7−15.

32 W. Chen, A. A. Said, Z. Wang, Y. Zhou, W. Liu, W. Gao, M. Liu, Q. Zhang, *ACS Appl. Energy Mater*, **2019**, DOI: 10.1021/acsaem.9b00857

33 V. Gonzalez-Pedro, E. J. Juarez-Perez, W. S. Arsyad, E. M. Barea, F. Fabregat-Santiago, I. Mora-Sero, J. Bisquert, *Nano Lett.* **2014**, *14*, 888-893.

34 A. Cualesh, T. Moehl, N. Tetreault, J. Teuscher, P. Gao, M. K. Nazeeruddin, M. Grätzel, *ACS Nano* **2014**, *8*, 362-373.

35 Z. Wei, H. Chen, K. Yan, S. Yang, *Angew. Chem., Int. Ed.* **2014**, *126*, 13455-13459.

36 S. S. Al Neyadi, A. A. Salem, M. A. Ghattas, N. Atatreh, I. M. Abdou, *Eur. J. Med. Chem.* **2017**, *136*, 270-282.

37 D.-R. Dauer, D. Stalke, *Dalton Trans.* **2014**, *43*, 14432–14439

38 F. H. Isikgor, B. Li, H. Zhu, Q. Xu, J. Ouyang, *J. Mater. Chem. A* **2016**, *4*, 12543-12553.

Entry for the Table of Contents (Please choose one layout)

Layout 1:

FULL PAPER

Benzothiazole modified naphthalene diimides NDI-BTH1 and NDI-BTH2 were successfully applied as electron transport layers in perovskite solar cells. The PSCs results are in good agreement with the OFET results. The highest power conversion efficiency (η) of 15.4% was obtained for the NDI-BTH2 ETL thin-film due to its excellent short circuit current (J_{sc} = 22.13 mA/cm^2) and open circuit voltage (V_{oc} = 0.98 V).

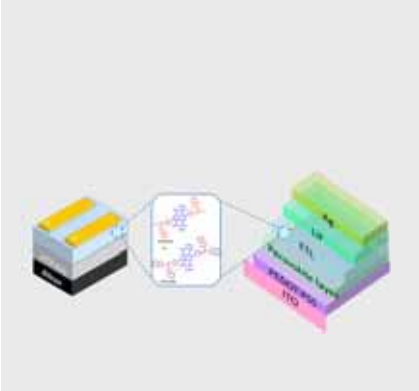

Dada B. Shaikh, Ahmed Ali Said, Dr. Zongrui Wang, Dr. Pedada Srinivasa Rao, Dr. Rajesh S. Bhosale, Adrian M. Mak, Kexiang Zhao, Yu Zhou, Wenbo Liu, Weibo Gao, Dr. Sidhanath V. Bhosale, Prof. Sheshanath V. Bhosale,* Prof. Qichun Zhang**

Page No. – Page No.

Influences of Structural Modification of Naphthalenediimides with Benzothiazole on the Organic Field-Effect Transistor and Non-Fullerene Perovskite Solar Cell Characteristics